

Icing Effect Experiments on the NASA High-Lift Common Research Model

Simon Prince[1], David MacManus[1], Davide Di Pasquale[1], Abhay Vincent[1], Ankit Sharma[1], Steven Daniels[1]

Kolleen K. Hood[2],

Melissa B. Rivers[3], Courtney Spells Winski[3], Thomas A, Ozoroski[4]

Paul White[5], James Brown[5]

Stuart Gates[6], Matthias Schulz[6], Constantin Jux[6], Harald Quix[6], Guido Dietz[6]

[1]Cranfield University, Bedfordshire, MK43 0AL, UK

[2]The Boeing Company, Seattle, WA 98124, USA,

[3]NASA Langley Research Center, Hampton, VA 23681 USA, [4]NASA Glenn Research Center, Cleveland, OH 44135, USA

[5]Airbus, Filton, Bristol, BS34 7PA, UK

[6]European Transonic Windtunnel (ETW) GmbH, Ernst-Mach-Strasse, 51147 Köln (Cologne), Germany

Abstract

Aircraft icing continues to pose a challenge for aircraft design and certification. Appendix O Supercooled Large Droplet (SLD) icing, particularly Freezing Rain, has been shown to be a challenge for industry due to the complex icing physics and regulatory landscape [1]. Though there are no validated computational tools or icing tunnels that can simulate the full range of Appendix O icing conditions, an experiment was developed to obtain aerodynamic data from a dry gaseous N_2 wind tunnel using artificial ice shapes generated with tools that would be representative of a typical airplane design process that manufacturers would use today. This paper presents findings from the EPSRC ICED-CRM campaign, which follows the aforementioned methodology using the 2.7% full-span NASA Common Research Model High Lift configuration in the European Transonic Wind Tunnel (ETW). Dry, Appendix C, Appendix O, and full-span runback ice shape configurations were tested at a range of Reynolds number and Mach numbers. Artificial ice shapes were generated using numerical icing tools under full-scale icing conditions and then tested in high Reynolds number conditions representative of flight. This approach allows the aerodynamic effects of icing to be examined systematically in terms of lift, drag, pitching moment, hysteresis, and sensitivity to Mach and Reynolds number. While the data presented in this paper is interim data, this study will provide a new validation dataset for a representative and publicly available large transport aircraft geometry. In doing so, it improves understanding of supercooled large droplet icing effects, supports validation of computational tools, and helps strengthen the experimental foundation for a future Appendix O certification method.

Keywords: Icing aerodynamics, Common Research Model, Experimental Aerodynamics

1. Introduction

Icing poses a significant challenge for aircraft design and certification. Even a small amount of ice can degrade an aircraft's aerodynamic performance and handling qualities, which is why icing is considered an integral part of modern transport airplane design [2]. Icing can occur when supercooled liquid water droplets in clouds strike exposed areas of the aircraft—such as the fuselage, wings,

engine nacelles, tail, and other surfaces where they can then freeze. Just a thin layer of ice can thicken the boundary layer, causing airflow separation, increasing drag, and lowering the stall speed. Runback ice resulting from an ice protection system causing ice to melt and re-freeze downstream, can form behind areas of protection and contribute to performance and handling qualities degradation. These effects are especially important for high-lift systems that rely on viscous interactions among multiple elements.

In order to certify an aircraft to operate in atmospheric icing conditions, an integrated approach is used that typically combines numerical simulations, icing tunnel tests, dry air wind tunnel tests, and flight tests. The atmospheric icing conditions used for transport airplane certification are covered in 14 CFR 25 and CS-25 Appendix C [5-6]. For small droplet icing, manufacturers identify critical and representative ice accretions on protected and unprotected surfaces and demonstrate that the aircraft can be safely operated with those accretions present. The evaluations account for assessment of residual, intercycle, runback, and failed-system ice shapes, as well as the effectiveness of ice protection systems.

For supercooled large droplet icing, the certification challenges increase significantly. Appendix O to 14 CFR Part 25 and CS-25 define Freezing Drizzle and Freezing Rain icing environments that overlap and extend beyond the droplet-size range represented by Appendix C [7,8]. The 1994 American Eagle Flight 4184 accident highlighted the safety implications of SLD-induced ridge ice and was a major driver for expanded SLD certification requirements [10]. Freezing rain is particularly difficult due to the large droplet sizes beyond 500μm. The physics of large droplet impingement, splashing, water-film transport, heat transfer, and delayed freezing are difficult to model and to reproduce experimentally at scale. Natural icing flight tests in SLD are expensive, operationally constrained, difficult to repeat, and rarely allow systematic isolation of Mach number, Reynolds number, or ice shape effects. For the design of next generation aircraft, these effects due to SLD need to be understood and considered during certification. Consequently, there is a need for high-fidelity aerodynamic datasets for Appendix O ice accretions under realistic flight-scale conditions. Manufacturers must consider the full Appendix O atmospheric envelope and demonstrate safe operation in Freezing Drizzle and Freezing Rain conditions. However, compared with Appendix C icing, the experimental and computational basis for Appendix O compliance remains less mature. To date, no tools or icing tunnels have been fully validated to simulate the entire Appendix O envelope, especially for Freezing Rain. Despite the lack of validation in computational tools, it is necessary to make progress in understanding the effects of Appendix O Freezing Rain using today's tools and methods. To achieve this, dry air aerodynamic data at flight Reynolds numbers was desired.

Cryogenic wind tunnels provide a means of investigating these effects by testing flight-scale Reynolds numbers. By reducing the test gas temperature and increasing density, facilities such as the European Transonic Wind Tunnel (ETW) can obtain high Reynolds numbers on subscale models while maintaining the required Mach number. The NASA High-Lift Common Research Model, CRM-HL, provides a suitable open high-lift transport geometry for such investigations. The CRM-HL was developed as a representative transonic transport high-lift configuration to support experimental and computational research on realistic multi-element high-lift aerodynamics [11].

The EPSRC ICED-CRM project addresses the need for high-fidelity, iced, high-lift aerodynamic data by testing the 2.7%, Full-span NASA CRM-HL model in ETW. The campaign includes clean (un-iced), Appendix C, Appendix O, and runback ice configurations. The artificial ice shapes are generated using numerical icing tools at full-scale icing conditions, including Freezing Rain cases representative of Appendix O, and are then scaled and manufactured for attachment to the wind-tunnel model using innovative techniques. This approach enables controlled dry, aerodynamic testing of representative ice accretion geometries.

The objective of the present paper is to summarize the preliminary experimental results from the ICED-CRM ETW campaign and to assess the aerodynamic effects of clean (un-iced), Appendix C, Appendix O, and runback ice configurations on the NASA 2.7% Full-span CRM-HL model. By combining representative full span, high-lift configuration, Appendix C and Appendix O ice shapes,

and cryogenic testing at flight-relevant Mach and Reynolds numbers, the ICED-CRM dataset provides a basis for improved understanding of iced high-lift aerodynamics, validation data for computational methods, and future certification approaches for SLD icing.

2. Background

2.1 Appendix O, SLD icing, and Freezing Rain difficulty

Appendix O extends the certification icing envelope to include SLD environments associated with Freezing Drizzle (FZDZ) and Freezing Rain (FZRA) [6, 7]. Instead of freezing immediately near the leading edge, droplets may splash, bounce, coalesce, form water films, run back, and freeze downstream. The physics of SLD presents several technical challenges like the need for validated computational tools for prediction, experimental capabilities for accurate simulation of SLD icing which are validated, the need to define operational encounter complexity and severity for SLD scenarios, improved icing detection and discrimination technologies and the limited possibility of using flight tests for SLD encounters due to challenges associated with finding critical Appendix O conditions in-flight [2]. Freezing Rain presents a particularly difficult certification challenge. Large droplets can produce extensive runback before freezing. The final accretion depends on a coupled multiphase process involving droplet trajectory, impact dynamics, splashing, water-film flow, convective heat transfer, phase change, and ice protection system behavior. It is difficult to conduct flight tests at the required critical icing conditions within a natural icing environment. In the design cycle for a new aircraft, it is imperative to account for SLD-related aerodynamic effects early in the design process to ensure the final design is safe and compliant with regulations [6], [7], [14].

2.1.1 Freezing Rain Artificial Ice Shape Definition

Considering the above challenges and acknowledged gaps in the numerical modeling of SLD an FZRA ice shape was calculated for testing purposes in this study. Freezing rain with MVD greater than 40microns was selected by the consortia as it is most different to Appendix C with a more voluminous ice accretion extending further aft on the aircraft wing. The conditions selected for the ice accretion were at 17,000ft, Mach 0.40, C_L 0.436 which is a representative holding point for the type of aircraft which CRM-HL is to represent. An angle of attack case of 2.2 degrees was chosen. It may be noted that this altitude was selected for commonality with the Appendix C ice shape, but it is above the envelope for FZRA, however the impact of this is small and does not impact the ice shape significantly. These flight conditions have been simulated in 3D CFD with the Tau RANS code based on an unstructured mesh for the purpose of generating a series of 2D pressure cuts through the wing to feed into the IGLOO2D ice accretion code. IGLOO2D was developed by ONERA in part to address the extension of the classical Appendix C envelope toward SLD, ice-crystal, and mixed-phase conditions [9]. The code is organized into dedicated components covering grid generation (MESH2D), the aerodynamic flow solution (AERO2D), droplet and ice-crystal trajectories (TRAJ2D), and ice accretion (ACCRET2D) [9]. The aerodynamic field is obtained by combining an external-flow solution with a dedicated boundary-layer calculation that supplies the wall quantities, in particular the convective heat transfer, required by the accretion module, and the trajectory module provides both Lagrangian and Eulerian formulations including the SLD wall-interaction effects relevant to Appendix O [9]. The SLD ice shape was calculated using the 10-bin discretization of the FZRA>40 distribution as defined in DOT/FAA/AR-09/10, with a temperature of 267K. This temperature was selected as will result in glaze ice shapes, but also implicitly defines the LWC of 0.23g/m^3 based on CS-25 Appendix O Figure 4. From these 2D ice shapes a lofted surface was created across the wing to generate the ice shape using CATIA.

2.2 Mach-number effects and high-lift compressibility

High-lift transport configurations can exhibit significant compressibility effects even at approach freestream Mach numbers. The slat suction peak may generate local supersonic flow and shock/boundary-layer interaction. The resulting shock position and pressure recovery influence maximum lift, stall onset, and buffet characteristics. Ice accretion can alter these mechanisms by changing local curvature, increasing effective roughness, thickening the boundary layer, or producing separation upstream of or near a shock [3, 4].

Mach-number effects are therefore coupled with Reynolds-number effects in iced high-lift aerodynamics. A change in Mach number may alter the slat suction peak and shock strength, while a change in Reynolds number may alter boundary-layer thickness, transition, and separation resistance. For iced configurations, these effects interact with the ice geometry. A runback ridge on or near the slat may have different aerodynamic consequences depending on whether the local flow is subcritical, transonic, or shock dominated. Similarly, ridge-induced separation on the main element may interact differently with the flap wake as Mach and Reynolds number vary [3], [4], [15].

Conventional low-speed or moderate-Reynolds-number wind tunnels cannot fully isolate these effects. Testing at flight-relevant Mach and Reynolds numbers is therefore necessary to determine whether observed aerodynamic penalties are caused primarily by ice geometry, Reynolds-number scaling, compressibility, or interaction. Cryogenic facilities such as ETW are well-suited to this task because they can vary the Reynolds number through temperature and pressure while maintaining the desired Mach number.

2.3 Swept-wing icing and CRM-based studies

Although airfoil studies provide the foundation for iced-aerodynamic understanding, realistic transport aircraft require three-dimensional swept-wing data. Swept wings introduce spanwise flow, crossflow instability, attachment-line effects, nonuniform accretion, and complex separation patterns. The aerodynamic penalty of an ice shape may vary strongly along the span because of changes in local chord, sweep, pressure distribution, and high-lift element loading [3, 4]. The CRM-HL configuration provides a further step toward realistic high-lift icing assessment as it is a representative high-lift configuration for transonic transport research. Because geometry is publicly available and widely used, it provides a strong basis for generating open, validation-quality aerodynamic datasets. The ICED-CRM project builds on this foundation by using an Appendix C, and introducing an Appendix O, and runback-ice configurations to the full-span CRM-HL model and testing them under cryogenic ETW conditions.

2.4 Aerodynamic hysteresis in iced high-lift configurations

Aerodynamic hysteresis occurs when the aerodynamic state depends on the direction of the angle-of-attack sweep. In separated flows, pitch-up and pitch-down sweeps may produce different lift, drag, and moment histories because separation and reattachment occur at different angles. Hysteresis is commonly associated with leading-edge separation, shock-induced separation, laminar-separation bubbles, large-scale wake dynamics, and stall-cell formation. Icing can intensify hysteresis by fixing or promoting separation at specific geometric features. A runback ridge, for example, may trigger separation during pitch-up at a particular chordwise location. During pitch-down, reattachment may not occur until a significantly lower angle of attack, creating a hysteresis loop in lift, drag, and pitching moment. In high-lift systems, this behaviour may be further complicated by slat wake interaction, flap separation, shock motion, and three-dimensional stall progression [15]. Public datasets documenting hysteresis for clean, Appendix C, and Appendix O high-lift configurations at flight-relevant Mach and Reynolds numbers remain limited. The ICED-CRM ETW campaign, therefore, provides an opportunity to examine hysteresis under conditions directly relevant to SLD certification and computational-method validation.

2.5 Research gap and contribution of the present work

Existing swept-wing icing studies have advanced the field, but there remains a need for full-span high-

lift datasets that combine realistic transport geometry, Appendix C and Appendix O ice shapes, and flight-relevant Mach and Reynolds numbers [16]. The present work addresses this gap through the ICED-CRM ETW campaign. The experiment uses the 2.7% full-span NASA CRM-HL model with clean, Appendix C, Appendix O, and runback ice configurations. The ice shapes are generated using numerical icing tools at full-scale icing conditions, including a representative Freezing Rain case, and are tested in dry air aerodynamic conditions in ETW. The resulting dataset enables systematic assessment of aerodynamic hysteresis, Mach-number effects, and Reynolds-number effects for iced high-lift configurations. This provides new data for understanding SLD/Freezing Rain aerodynamic penalties, validating computational methods, and supporting future certification approaches for Appendix O icing. The data will be made available openly, on both the NASA CRM online data archive and the UK National Wind Tunnel Facility data archive.

3. Experimental Methodology

The 2.7% NASA High Lift CRM full span model was tested in the European Transonic Wind Tunnel (ETW). The ETW is the premier European cryogenic and pressurized aerodynamics test facility. The tunnel employs nitrogen gas cooled to temperatures as low as 110K, and pressurized up to 4.5 bar. With this capability, the facility can simulate experimentally the physics of air flow up to full flight Reynolds numbers for typical narrow body and wide body airliners using sting mounted full models and wall mounted half-span models. The facility employs an adaptive nozzle system, slotted wall liners and diffuser flaps to enable precise control of Mach number in the subsonic, transonic regime, and moderate supersonic (down to milli-Mach accuracy). Measurement systems available include static and dynamic pressure model and wall pressure measurement, static and dynamic pressure and temperature sensitive paint, sting mounted 6-component force and moment measurement and optical aeroelastic deformation measurement.

Figure 1 shows the 2.7% full span high lift CRM model in the test section of the ETW with clean (un-iced) wings, deployed leading edge slats and flaps. This model has a wing semi-span of 31.23 inches and a mean aerodynamic chord of 7.45 inches. Full span reference area and length, for force and moment non-depersonalization, was 3.01 square feet (semispan of 1.51 square feet) and 5.21 feet respectively. The model incorporated 315 static pressure taps distributed across nine spanwise wing stations as well as 12 Kulite dynamic transducers. The full details of the model geometry and sensor details are provided in reference [18].

Details of the leading edge ice shapes are presented in Figures 2 and 3, along with indications of where these were located on the model, which correspond with notional sections of the leading edge slats and surfaces that would not have ice protection, which was defined by the CRM-HL Ecosystem in order to be somewhat representative of modern airliners and provide the ability to test for Reynolds number effects. These include the inboard strake/onglet, the inboard slat and engine pylon intersection, and the outboard slats. The Appendix C ice shapes, indicated in Figure 2 were those described in the literature [17] and were provided by Boeing, which employed additive manufacturing to fabricate the components which were bonded to the cryogenic wind-tunnel model with an appropriate epoxy adhesive. The Appendix O parts, provided by Cranfield University, were cast in molds out of CAF-1 silicon sealant material and bonded to the surface using the same silicon material. Both materials were chosen for their thermal expansion properties to survive repeated cooling / warm-up cycles, but experience during the tests showed that silicon was not robust enough for prolonged testing at cryogenic conditions. The details of how the Appendix O leading edge ice geometries were computed have been described in section 2.1.1. All leading-edge ice parts were treated with bonded roughness elements to simulate the scaled roughness of the ice as appropriate for their conditions per regulatory guidance (AC 25-25A and AC 25-28). For instance, F70 grade carborundum particles were applied to the surface of the Appendix O silicon parts.

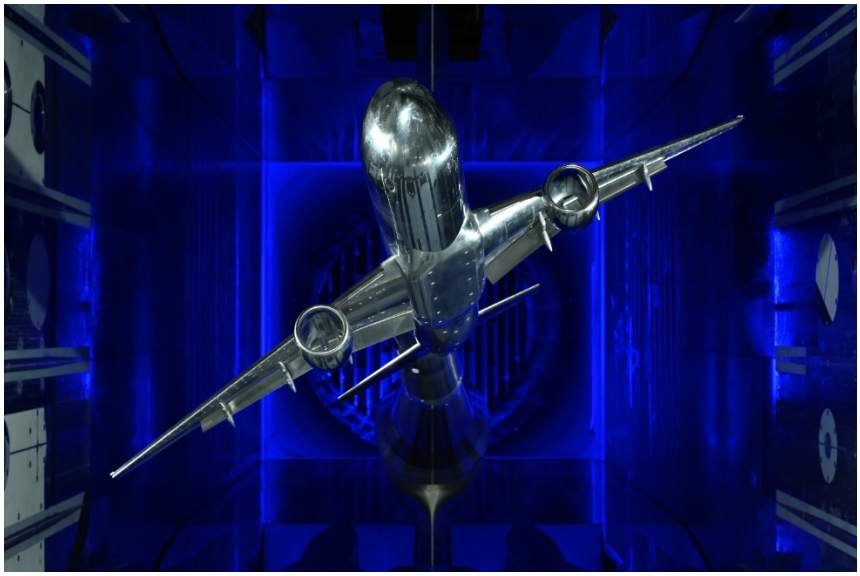


Figure 1 – The 2.7% scale NASA High-Lift CRM model in clean configuration in the ETW test section (Credit: ETW)

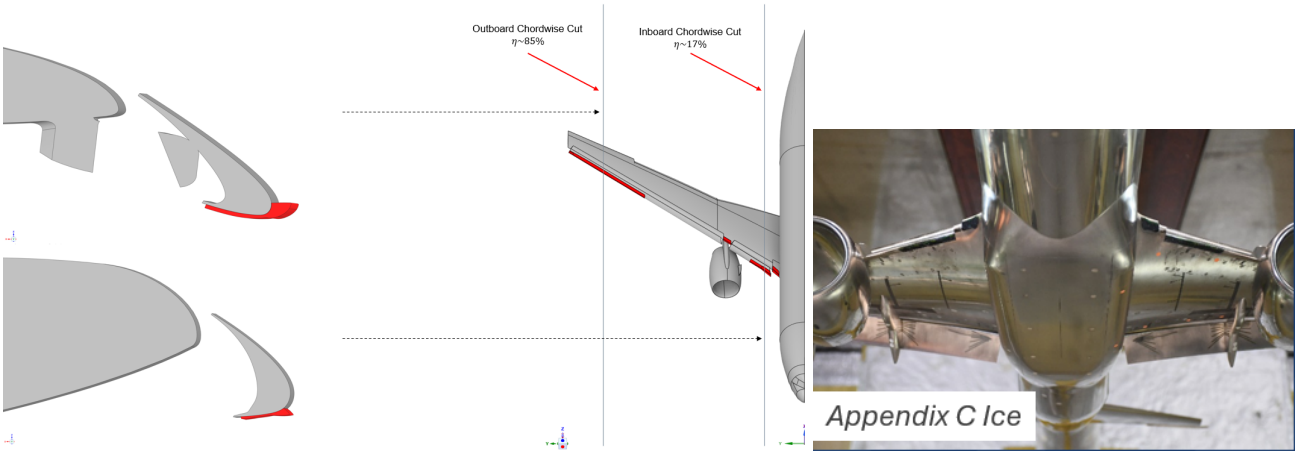


Figure 2 – The Appendix C leading edge ice shapes (highlighted in red) used in the test, applied to the 2.7% NASA High-Lift CRM model (Credit: ETW).

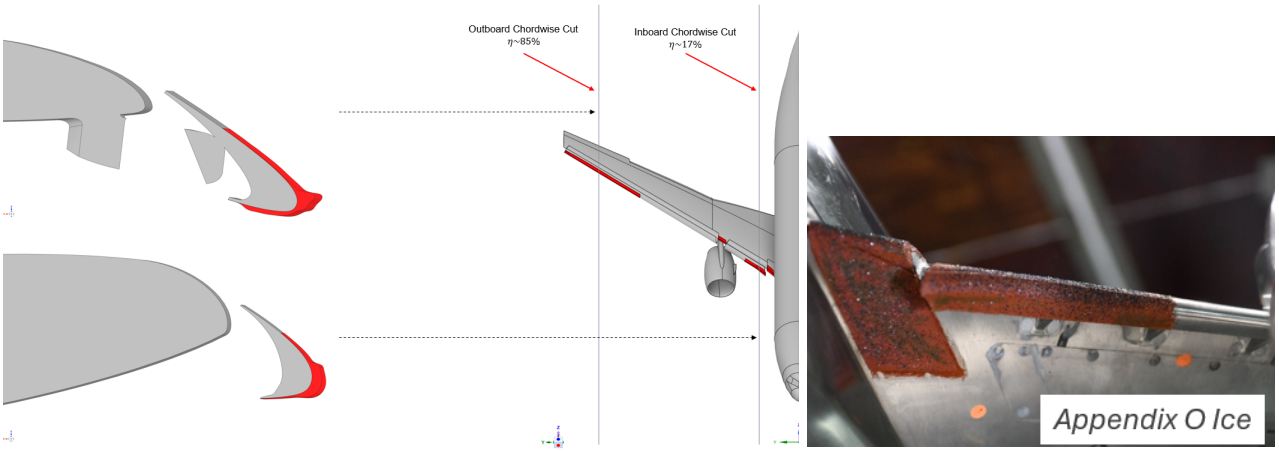


Figure 3 – The Appendix O leading edge ice shapes (highlighted in red) used in the test, applied to the 2.7% NASA High-Lift CRM model (Credit: ETW).

The planned experimental test matrix was defined in order to resolve the following aerodynamic effects:

i) The effect of Reynolds number, at constant Mach number, on the aerodynamic performance and handling qualities (including pitching moment and lateral-directional stability) impact of leading-edge ice alone as well as with runback ice ridges of different heights and positions on the slats behind the ice-protected leading edges.
ii) The effect of Mach number, at constant Reynolds number, on the aerodynamic performance and handling qualities (including pitching moment and lateral-directional stability) of the same configurations.
iii) The effect of leading-edge ice on aerodynamic hysteresis in pitch.

Data were acquired during continuous pitch sweeps, at a low angular speed of 0.15° per second, which was confirmed to provide identical force and moment and pressure data as acquired using a pitch-pause approach. This allows significantly reduced test times and associated financial cost per pitch polar. The model was predominantly tested in an "inverted" position to achieve the full α range, and the test runs at the highest Reynolds number / pressure conditions were performed first for cost efficiency. For selected configurations, a flow angularity run was performed by rolling the model to an upright orientation and testing across a reduced α range (due to sting movement limitations). Every run was repeated in a back-to-back fashion to obtain near-term repeatability. Table 1 presents the matrix of test conditions planned for the test. It was decided, during the test, that the achieved 16 million Reynolds number conditions (representative of the CRM-HL flight scale Reynolds numbers) would have been too challenging for the Appendix O and runback ice cases where there was a greater risk that these parts would fail.

Table 1: Matrix of test conditions for the planned test.

	Re_c ($x10^6$)						
Test blocks	1.6	3.33	5.32	8	10	12	16
Clean (no ice)	x	x	x	x	x	x	x
LE Appendix C (App C)		x	x		x	x	x
LE Appendix O (App O)		x	x		x	x	x
App O + Runback 1		x	x		x	x	x
App O + Runback 2		x	x		x	x	x
App O + Runback 3		x	x		x	x	x
App O + Runback 4		x	x		x	x	x

Figure 4 presents, for the Mach 0.2 cases, the plot of the test conditions at the three stagnation temperatures used in the test. The strategy was to obtain data for five Reynolds numbers at full cryogenic, T_0 = 117K condition, and two in ambient warm condition, as well as one for 8 million Reynolds number at the intermediate stagnation temperature of 154K. This allowed the effect of model loading or wing deformation effects to be isolated for different dynamic pressures at a constant stagnation pressure and Mach number. Similar conditions were tested, but with a reduced number of points, at Mach numbers of 0.18, 0.22, 0.26, 0.30 and 0.35 in order to resolve the effect of Mach number at constant Reynolds number.
In order to reduce differences in installation effects, particularly sting interference, and to allow direct tunnel-to-tunnel comparison between NASA NTF data, both the NASA internal sting balance and the NASA NTF vertical tail sting connector were employed in the test. This was connected to the ETW sting, through which the balance wiring was passed to the data acquisition system and power source, located in the warmed environmental chamber on the model cart above the model working section. The pressure scanners were also maintained at ambient temperature in specially heated and thermally insulated chambers within the model fuselage.

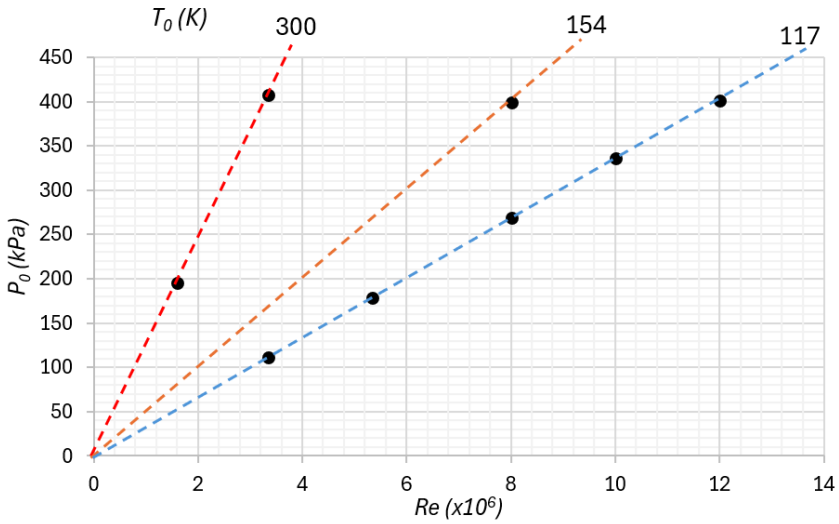


Figure 4 – Test points for M = 0.2: P_0 versus Reynolds number at three stagnation temperatures.

Testing of the metallic Appendix C shapes proceeded without any problems. During the testing itself, however, it was found that the CAF silicon material, tested as part of the project research question rather than as the usual method of approach, was not as effective as first thought, at surviving the intense cold of 117K and associated aerodynamic loading followed by the warm-up to near ambient temperatures. The first test block with the silicon ice parts resulted in small sections peeling off and being shed where the silicon was bonded to both the steel body and small cement filled regions, and also where an unsealed pressure tap probably imposed pressure on the material.

In order to ensure that definitive Appendix O leading edge alone data was acquired, with acceptable repeatability, without the interference effect of damaged ice parts. A second repeat run was therefore undertaken, which successfully acquired data without significant ice damage or shedding taking place until the very final pitch traverse. The repeatability between the two sets of data prior to silicon shedding was found to be good enough to give confidence that the second set of Appendix O data was acceptable. Given the challenges with the silicon-based Appendix O parts, it was decided to pivot the testing to full-span runback testing by removing the Appendix O shape.

It was decided to devote the remaining test time to acquire accurate data on the detailed Reynolds number effects on different heights of full-span runback ice alone, for a notional 4% scale aircraft with full span leading edge ice protection system. This Figure comes from an additional scaling factor of 65% to tie in to other industry work in icing, such as on the NASA CRM65 and future Appendix O industry work. Table 2 presents the actual achieved test matrix during the testing that took place between 7th – 24th April 2026. This paper will present only the results of the study of leading-edge ice alone, and a separate paper will present the results of the runback ice study.

Table 2: Matrix of test conditions measured during the actual test.

	Re_c (x10^6)						
Test blocks	1.6	3.33	5.32	8	10	12	16
Clean (no ice)	x	x	x	x	x	x	x
LE Appendix C (App C)		x	x		x	x	x
LE Appendix O (App O)			x		x	x	
20mm full-span runback		x	x		x	x	
50mm full-span runback		x	x		x	x	
30mm full-span runback		x	x		x	x	

3. Results and Discussion

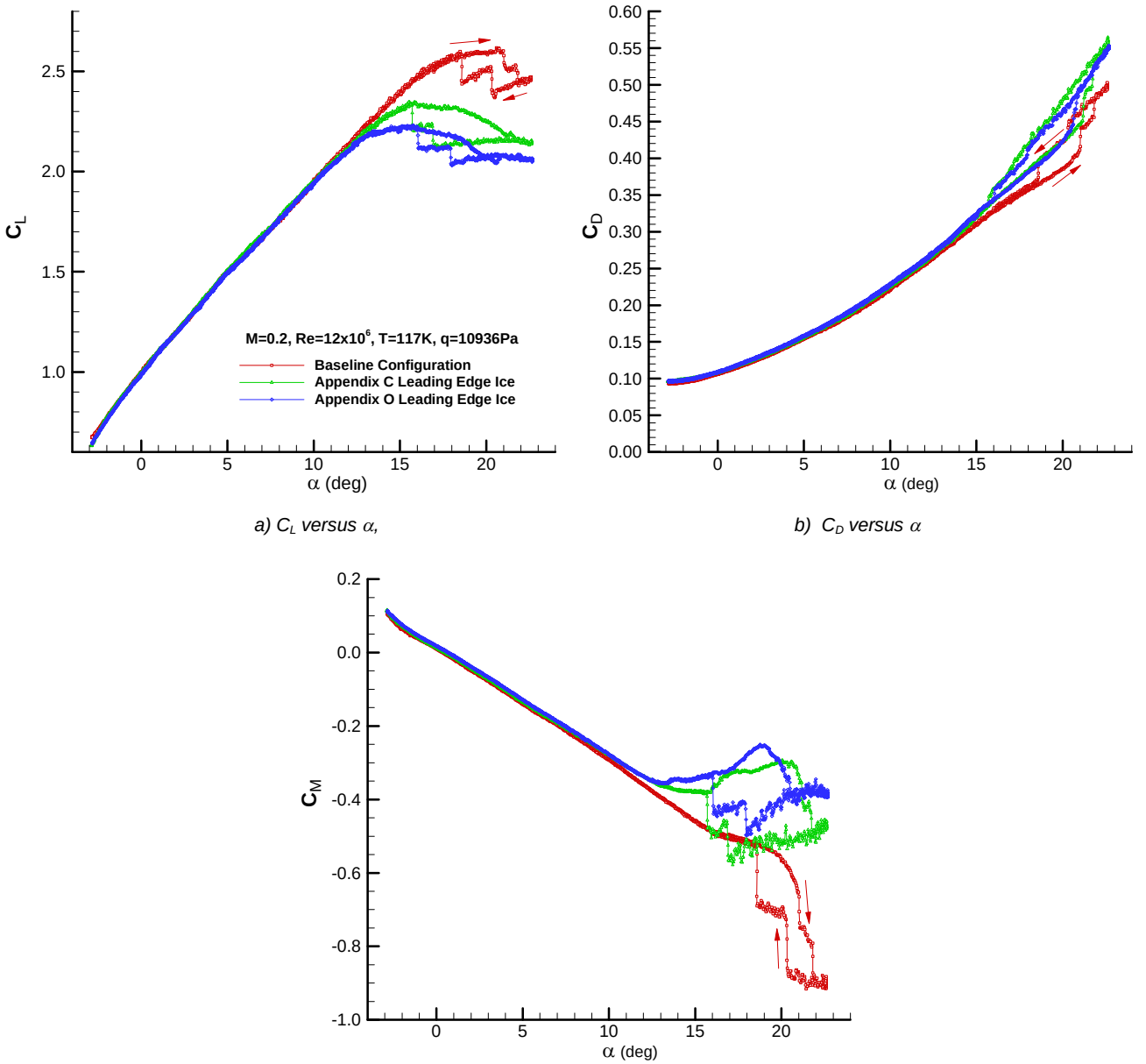
It should be noted that the preliminary data presented in this paper, at the time of writing, was corrected for wall / buoyancy effects, but the preparation of the final definitive data is currently ongoing. The data presented is therefore of an interim nature.

The aerodynamic effects of the two types of leading-edge ice shapes for the Mach 0.2, 12 million Reynolds number condition are clearly seen in the comparisons of C_L, C_D and C_M versus α, plotted in Figure 5, for the pitch up – down runs. What is immediately evident is the large difference in C_{Lmax} between the three cases. The effect of Appendix C leading edge ice (in green) is to drastically reduce the maximum C_L to 2.3, and the angle of attack at which it occurs at around α =15°. The situation is even worse in the case of Appendix O leading edge ice (in blue). While the lift trend for this class of ice is similar to that measured for Appendix C, the C_{Lmax} is seen to drop further, to 2.2, but the angle of attack at which this occurs is about the same.

Here the effect of pitch hysteresis is also clearly evident. For the baseline clean configuration (in red), C_L rises on the pitch-up and then plateaus to a maximum of 2.6 at around α =19° before a two-stage stall occurs, whereby one wing stalls before the other. On the pitch-down, the lift-hysteresis manifests itself in a later two-stage recovery, where one wing recovers before the other, before C_L returns to the original trend. The effect of Appendix C ice is seen to extend, by almost double, the α – range of the lift hysteresis, where recovery to the initial pitch-up trend occurs at α =15.5°. On the pitch up asymmetric stall was evident in the rolling moment rather than in lift data, but the lift recovery does exhibit evidence of an asymmetric recovery of attached flow on the wings. With the Appendix O ice the extent, in α, of the lift hysteresis, is the same as with the Appendix C case. As expected, due to the greater surface extent of the Appendix O leading edge ice, this class of ice is more penalizing than the Appendix C type.

Hysteresis is also seen in the measured drag coefficient characteristics between the pitch-up and the subsequent pitch-down data, but care must be taken in interpreting this preliminary data. The wing separation derived drag rise, for the baseline clean configuration is seen to occur at α =21° on the pitch-up (corresponding with the lift stall), whereas on the pitch-down the recovery occurs at α =18°. The drag characteristics for both the Appendix C and Appendix O leading edge ice configurations appear very similar, with earlier upwards divergence from the baseline drag trend, a significantly higher post-stall C_D level, and a more extensive hysteresis range before a later recovery to its initial pitch-up trend. Interestingly the drag rise caused by Appendix O ice configuration occurred near one degree angle of attack earlier than that caused by Appendix C leading edge ice, but post stall C_D level was slightly higher for the Appendix C ice configuration.

This may change once the remaining sting related corrections are accounted for. The pitching moment characteristics are equally interesting and also exhibit strong pitch-hysteresis effects. For the baseline configuration, the linear pitch trend breaks at around α = 16°, due to the onset of wing boundary layer separation beginning to affect leading edge suction. The main nose-down pitch break is seen to begin at around α = 20°, and like the corresponding lift characteristics, goes through a two-stage event. On the pitch-down the C_M recovers to its original pitch-up trend, through a two-stage process, at α = 18.5°. Both leading-edge ice configurations significantly modify the C_M characteristics, with both causing a destabilizing (positive C_M gradient) during the post-stall pitch-up. This is seen to be highest with Appendix O ice (blue curve). The break in the initial linear C_M trend with α occurs much earlier, at around α = 13° for both ice configurations, than seen without leading edge ice. The pitch-down C_M recovery in both ice cases exhibit the same two-stage characteristics as seen in the lift trends, but the average C_M level with Appendix O leading edge ice was significantly less (nose down) than that measured for the Appendix C ice shapes.



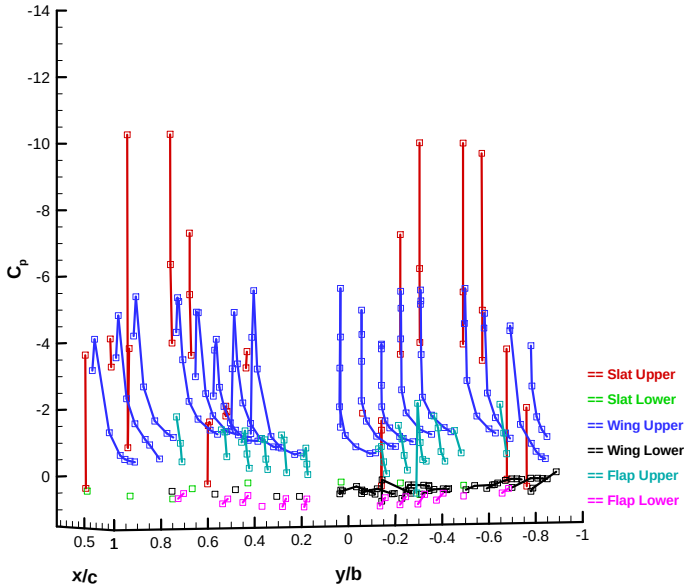
a) C_L versus α,

b) C_D versus α

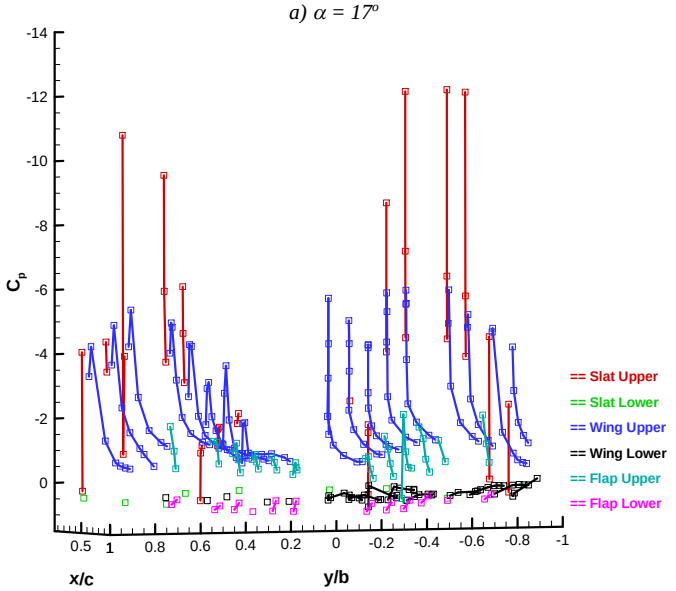
c) C_M versus α

Figure 5 – Comparison of measured forces and moments on pitch up and down, M=0.2, Re_c=12x10^6, T=117K, q = 10.9kPa (Note: this analysis is based on preliminary test data)

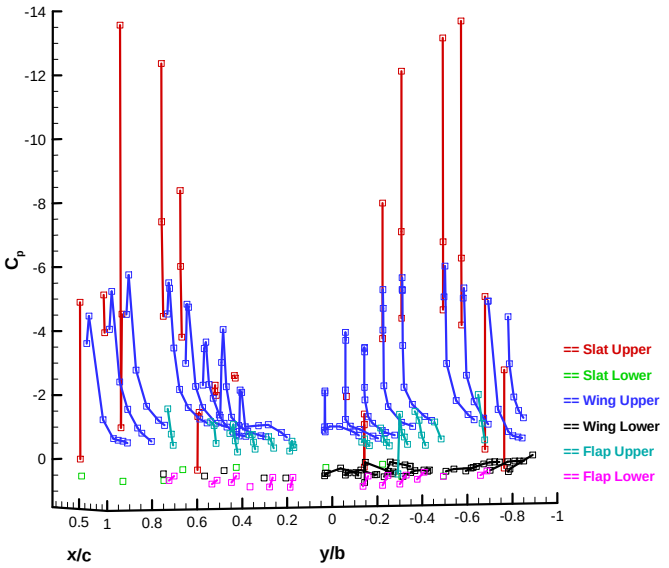
Examples of the measured C_p distributions on the CRM-HL clean (un-iced) model wings for three angles of attack on the pitch down during this same test, are presented in Figure 6. Here, the data for the port wing are on the left with positive values of *y/b*. The pressures on the different components are color coded with the high suctions (negative C_p's) on the slats evident in red. The details of the model and the pressure tapping locations are provided in reference [18], but the pressure tapping distributions are not symmetric between the port and starboard wings, as is evidenced in the plots. Detailed analysis of the pressure distributions will be undertaken and presented in future papers, but the first analysis made for this paper clearly showed that the two-stage stall / recovery is significantly associated with asymmetric separations on the wing and subsequent asymmetric degradation of wing circulation and slat suction.



a) α = 17º



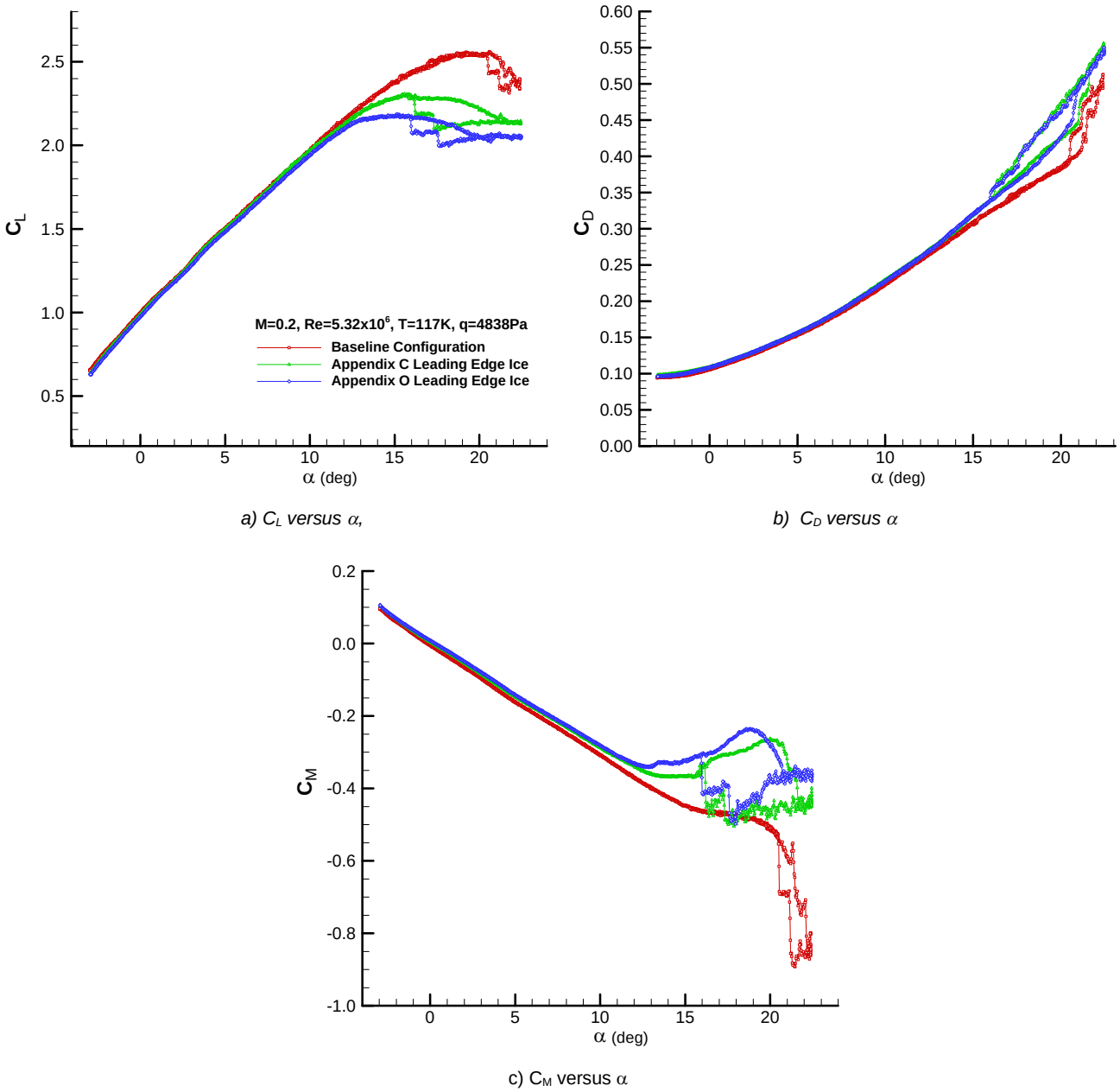
b) α = 19º



c) α = 21º

Figure 6 – Comparison of baseline measured wing surface pressure distributions on the pitch down, M=0.2, Re_c=12x10^6, T=117K, q = 10.9kPa. (Note: this analysis is based on preliminary test data)

Figure 7 presents corresponding force and moment comparisons, for pitch-up and down tests with hysteresis effects, at the same Mach 0.2 condition but at the lower Reynolds number of 5.32 million. Similar trends are apparent in this data for the lower Reynolds number, but interestingly the hysteresis range for the baseline model is considerably smaller, with recovery in lift on the pitch-down occurring at α = 20°, rather than at 18.5° for the 12 million Reynolds number case. The hysteresis range for the two leading edge ice configurations, however, seem to have been unaffected by the reduced Reynolds number.



a) C_L versus α,

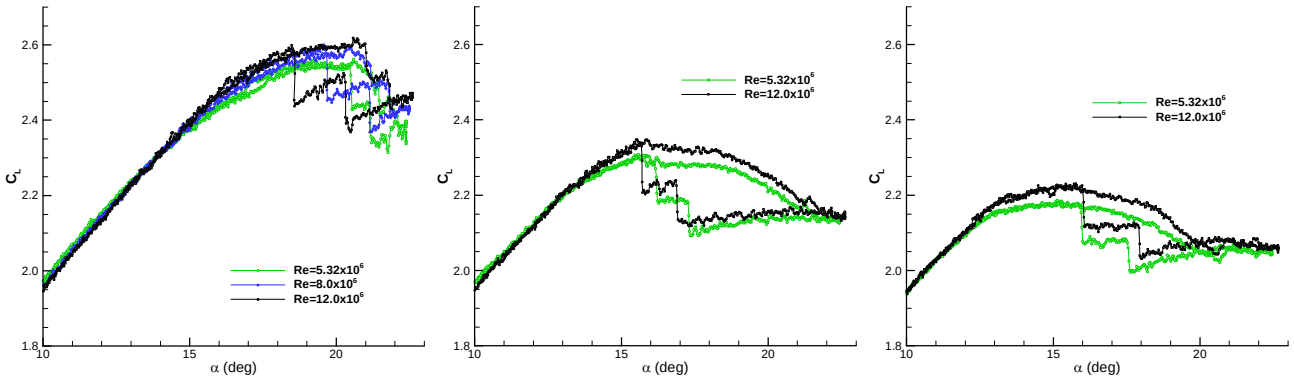
b) C_D versus α

c) C_M versus α

Figure 7 – Comparison of measured forces and moments on pitch up and down, M=0.2, Re_c=5.32x10^6, T=117K, q = 4.84kPa. (Note: this analysis is based on preliminary test data)

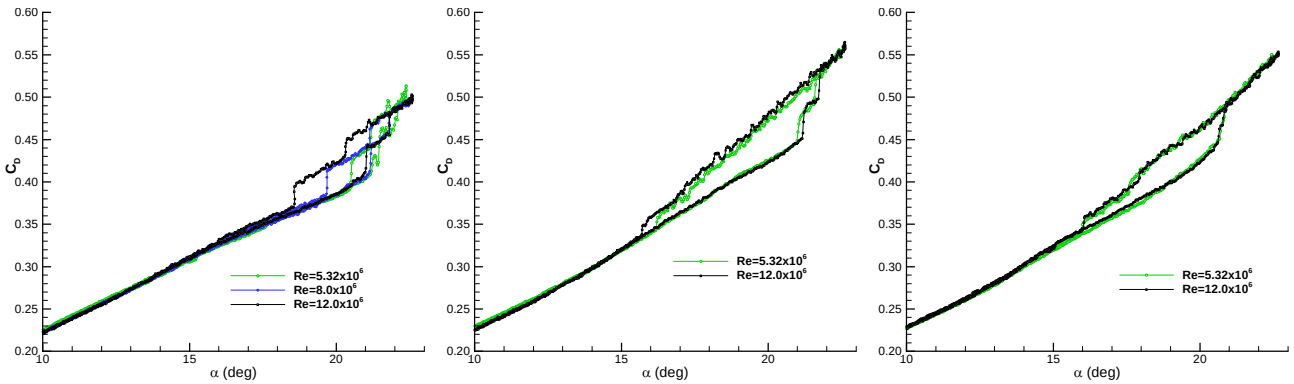
The effect of Reynolds number on the hysteresis effects on aerodynamic forces and moment for the three configurations are explored in the comparisons of Figures 8 -10. The variation of lift characteristics with Reynolds number is plotted in Figure 8, where the data for the baseline CRM-HL includes measurements for intermediate 8 million Reynolds number. Here it can clearly be seen that the effect of an increase in Reynolds number is to increase the extent of the lift hysteresis over a wider pitch range on the pitch-down. Since higher Reynolds numbers could not be attained in the present

test for Mach 0.2, it was not possible to ascertain the critical Reynolds number at which this effect reaches an equilibrium and the characteristics can be assumed to be that for full flight. The lift hysteresis for both leading-edge ice configurations appears to remain unaffected significantly by the change in Reynolds number in the range measured, although the effect of the ice in considerably delaying recovery to pre-stall levels on the pitch-down is clearly evident. Similar conclusions can be derived from the measured drag coefficient and pitching coefficient characteristics with angle of attack, plotted in Figures 9 and 10 respectively. The effect of Reynolds number on the initial break in pitching moment slope is evident with this occurring later, at higher angle of attack as Reynolds number is increased. Reynolds number is also seen to slightly increase the nose-down pitching moment level in the post-stall regime.



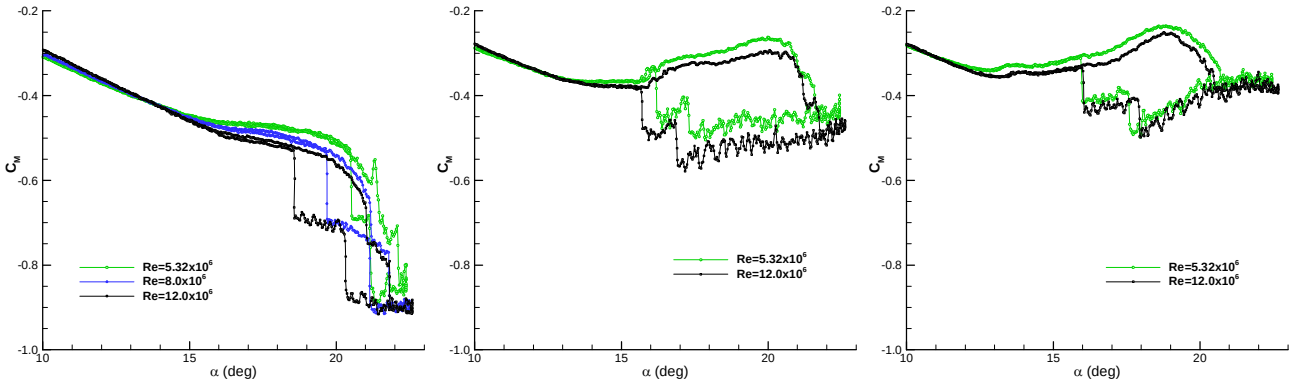
a) Baseline configuration *b) Appendix C Leading Edge Ice* *c) Appendix O Leading Edge Ice*

Figure 8 – Effect of Reynolds Number on lift coefficient on pitch up and down, M=0.2. (Note: this analysis is based on preliminary test data)



a) Baseline configuration *b) Appendix C Leading Edge Ice* *c) Appendix O Leading Edge Ice*

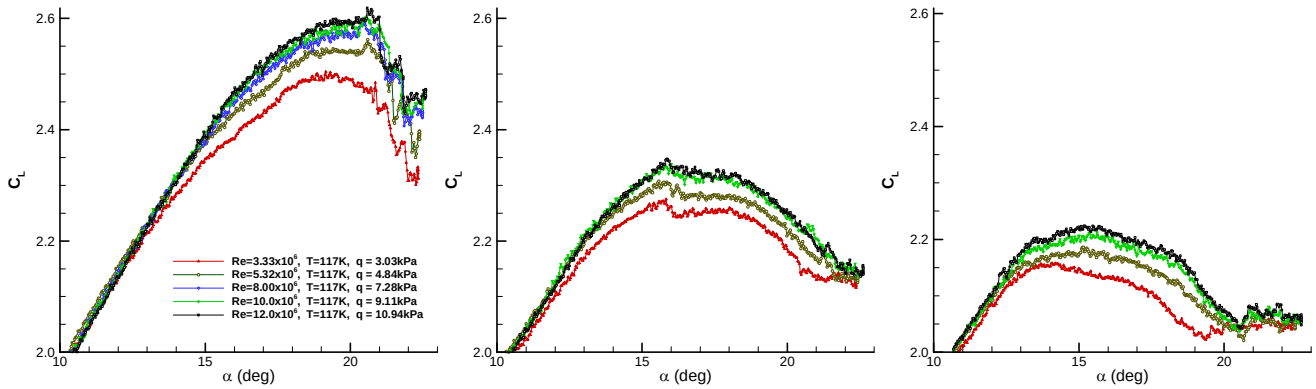
Figure 9 – Effect of Reynolds Number on drag coefficient on pitch up and down, M=0.2. (Note: this analysis is based on preliminary test data)



a) Baseline configuration *b) Appendix C Leading Edge Ice* *c) Appendix O Leading Edge Ice*

Figure 10 – Effect of Reynolds Number on pitching moment coefficient on pitch up and down, M=0.2. (Note: this analysis is based on preliminary test data)

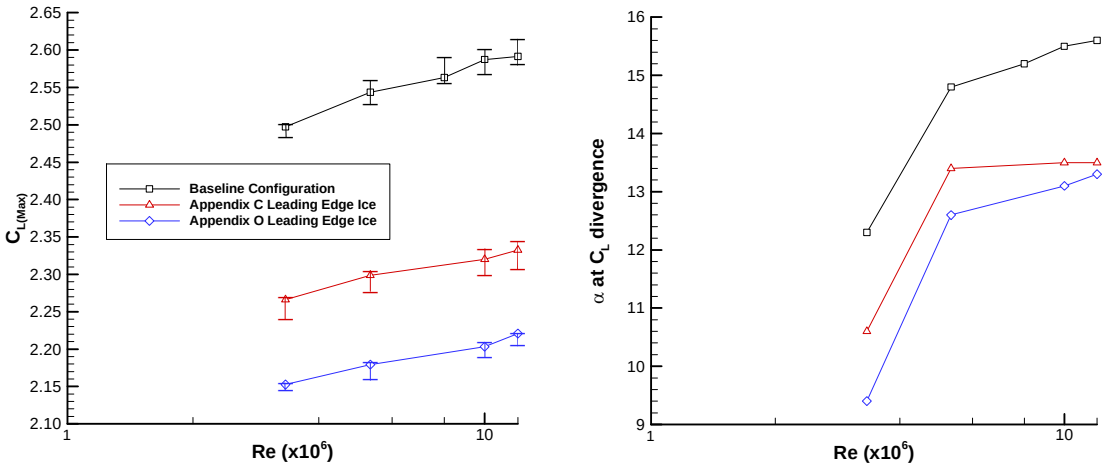
The effect of Reynolds number on the pitch-up lift curves, across a wider Reynolds number range for the Mach 0.2, T = 117K condition, is presented in Figure 11. Here data is plotted for five Reynolds numbers between 3.33 million up to 12 million. The effect of leading-edge ice in significantly reducing the level of C_{Lmax} is clearly evident, with Appendix O ice being more detrimental than Appendix C. The effect of Reynolds number is seen to be both an increase in C_{Lmax} with increase in Reynolds number for all three configurations, and a later divergence from the linear lift curve. Interestingly, there appears to be only a minimal increase in C_L level in the non-linear region, between Reynolds numbers of 10 million and 12 million.



a) Baseline configuration *b) Appendix C Leading Edge Ice* c) Appendix O Leading Edge Ice

Figure 11 – The effect of Reynolds number on measured C_L versus α, M=0.2, T=117K. (Note: this analysis is based on preliminary test data)

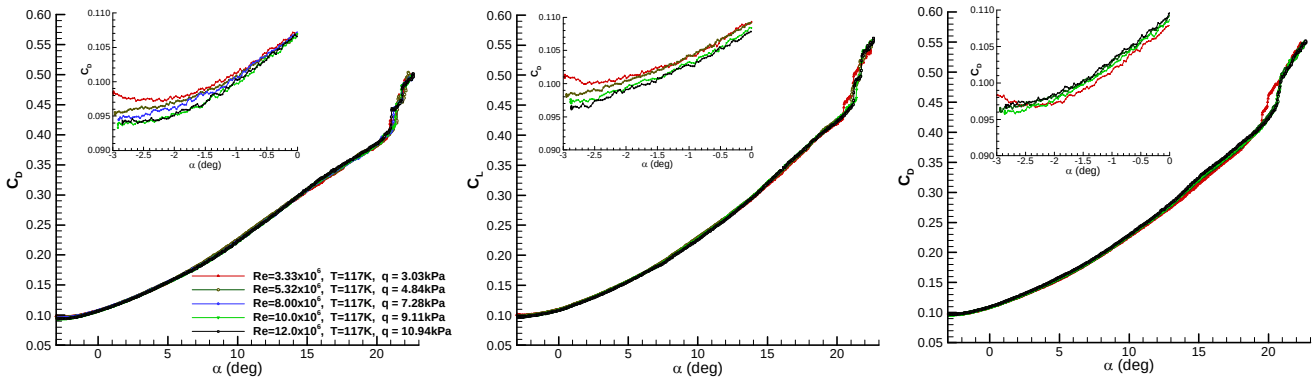
A more detailed analysis of the effect of Reynolds number on C_{Lmax} and the angle of attack at which the lift trend diverges from its initial linear slope, is provided in Figure 12 for this Mach 0.2 case. Here, C_{Lmax} versus α is plotted for a value averaged across the limited repeat runs undertaken (no more than 3), along with an indication of the maximum and minimum values across those repeat runs. This shows that increasing Reynolds number increases C_{Lmax} both without and with leading edge ice, and the greatest rise occurs at the lower Reynolds numbers. Between 10 and 12 million Reynolds number, there is still a rise in maximum C_L, for the two leading edge ice cases, but less so for the baseline case. Between 3.33 million and 5.32 million Reynolds number there is a big effect on the onset of lift divergence from the linear trend. Between 10 and 12 million the change in this onset angle of attack is much smaller for all three configurations.



a) $C_{L(max)}$ *b) α at divergence from linear C_L trend*

Figure 12 – The effect of Reynolds number on measured lift characteristics, M=0.2, T=117K. (Note: this analysis is based on preliminary test data)

The corresponding variation of drag coefficient with Reynolds number is plotted in Figure 13, with the low angle of attack data, including an indication of minimum drag, is shown as an inset plot, as this is where the greatest effect of Reynolds number occurs. Unlike lift, the data shows that there is very little effect of Reynolds number across the α range until the post-stall drag rises, and even there the effect of Reynolds number is not large. Removing the ideal induced drag component would be expected to reveal greater Reynolds number effects. In the negative alpha range, the C_D value increases as Reynolds number reduces. This is to be expected due to the increase in the relative thickness of the boundary layers, which will increase the displacement effect, and thereby form drag.

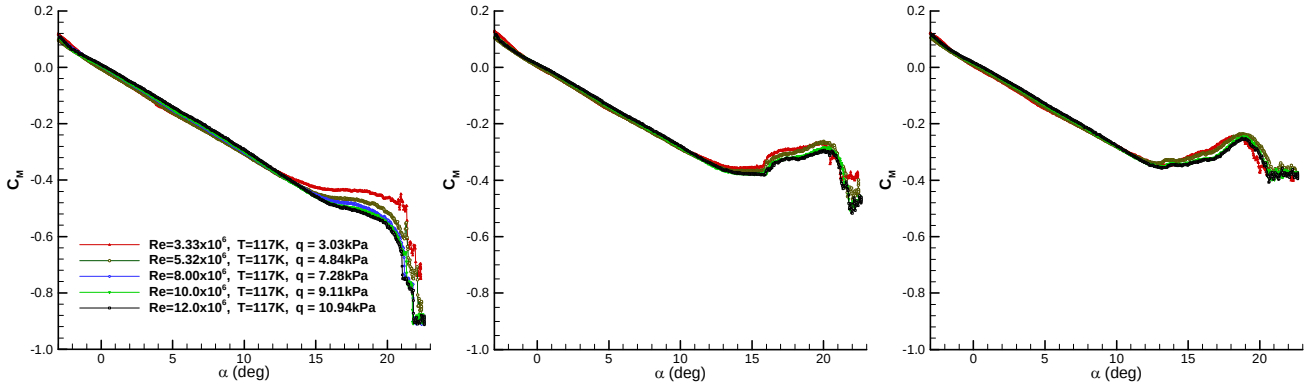


a) Baseline configuration *b) Appendix C Leading Edge Ice* c) Appendix O Leading Edge Ice

Figure 13 – The effect of Reynolds number on measured C_D versus α, M=0.2, T=117K. (Note: this analysis is based on preliminary test data)

The corresponding comparison of the effect of Reynolds number on the C_M characteristics is plotted in Figure 14. The effect of increasing Reynolds number on the baseline configuration is seen to delay to higher α, the onset of the divergence from the initial linear trend. The angle of attack at which the pitching moment break occurs seems not to have been affected by Reynolds number but the higher the Reynolds number, the higher the negative nose down C_M, until the results for 10 million and 12 million seem to have converged. The effect of both leading-edge ice configurations appears to reduce significantly the sensitivity of pitching moment to Reynolds number, particularly in the variation in C_M

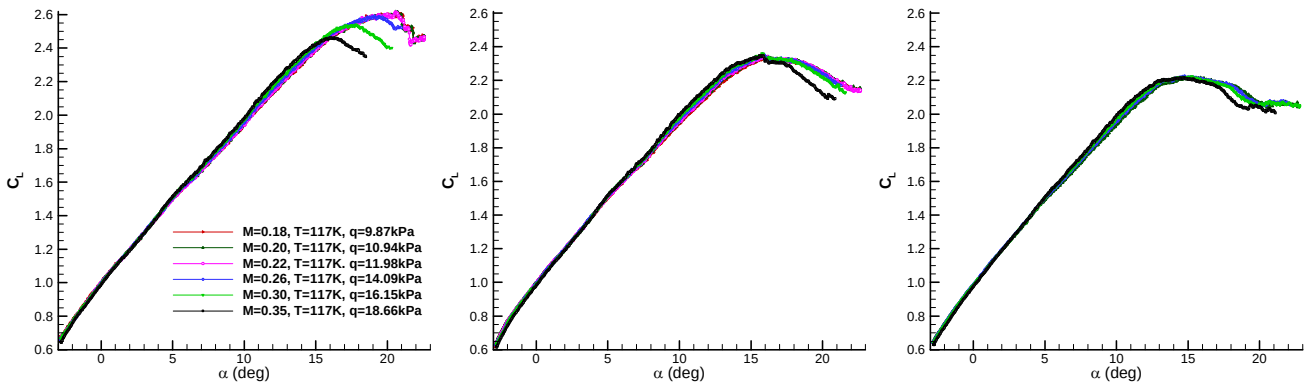
level in the post-linear region prior to pitching moment break. Leading edge ice is seen to reduce significantly the CM level in the non-linear α range and introduce a positive value of $dC_M/d\alpha$ prior to pitching moment break.



a) Baseline configuration *b) Appendix C Leading Edge Ice* c) Appendix O Leading Edge Ice

Figure 14 – The effect of Reynolds number on measured C_M versus α, M=0.2, T=117K. (Note: this analysis is based on preliminary test data)

The effect of Mach number at a fixed Reynolds number of 12 million is presented in Figures 15 – 17. Tests were performed at Mach numbers between 0.18 and 0.35 for the baseline configuration and for the two leading edge ice configurations. For C_L, plotted in Figure 15, Mach number is seen to affect C_{Lmax} level only for the baseline configuration, where increasing Mach number is seen to result in a later divergence from the linear lift trend, but an earlier lift stall above a Mach number of 0.22. With both configurations of leading-edge ice, the higher Mach numbers also result in a later divergence in the linear lift trend, but there is very little sensitivity of C_{Lmax} to Mach number. Detailed analysis of the pressure distributions on the wing, along with the calculation of the critical pressure coefficient on the slat, C_p*, is needed to highlight the physical cause of these trends.

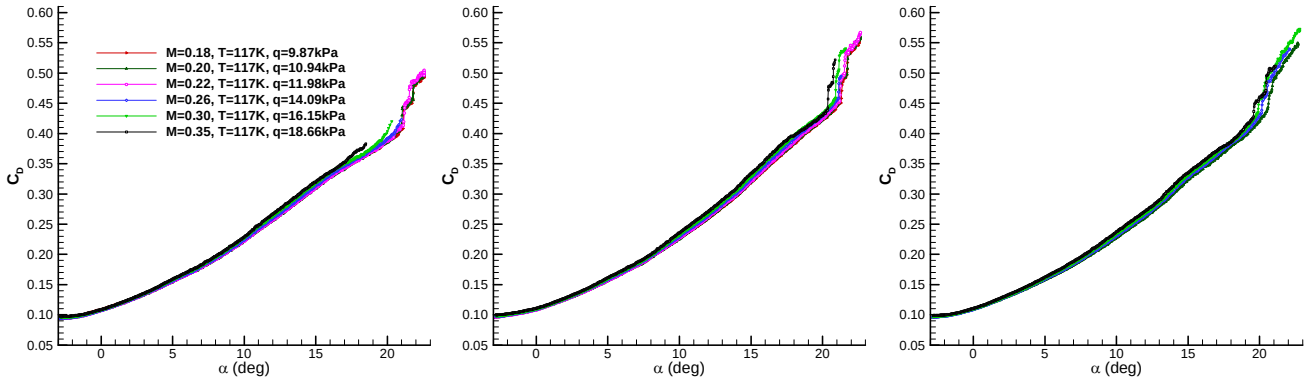


a) Baseline configuration *b) Appendix C Leading Edge Ice* c) Appendix O Leading Edge Ice

Figure 15 – The effect of Mach number on measured C_L versus α, Re=12x10^6, T=117K. (Note: this analysis is based on preliminary test data)

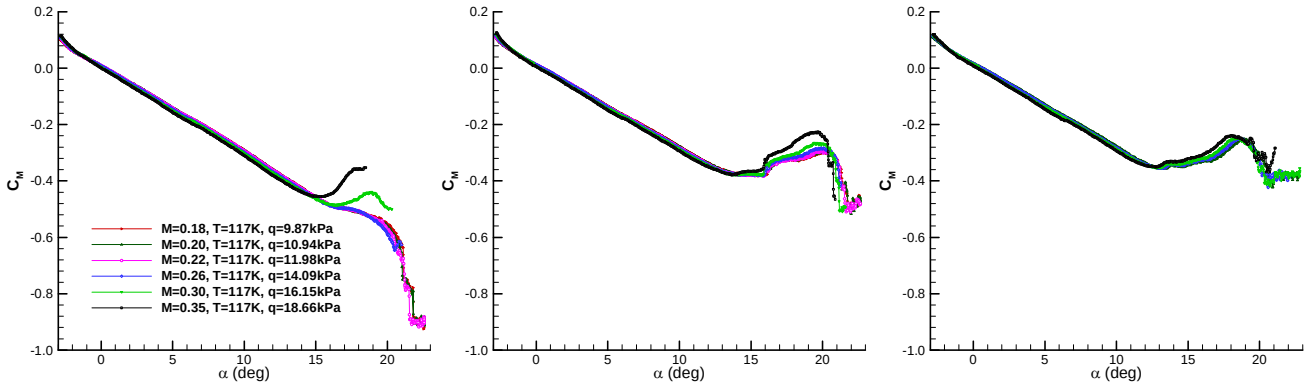
The corresponding comparisons for drag coefficient are plotted in Figure 16. Since this data is not yet finalized, no definitive conclusions can be made on these trends. Detailed analysis will need to be performed on the properly corrected data, to extract ideal induced drag components and assess any components due to the formation of shock waves on the slats, expected at the higher angles of attack and Mach number.

Finally, the corresponding pitching moment data are plotted in Figure 17. For all three cases, the C_M curves for the Mach numbers below M = 0.3 appear to be almost identical, within the bounds of experimental uncertainty. The data for Mach 0.3 and 0.35, however, shows that Mach number progressively induce an earlier unstable pitch break, although this effect is significantly weaker with leading edge ice installed.



a) Baseline configuration *b) Appendix C Leading Edge Ice* c) Appendix O Leading Edge Ice

Figure 16 – The effect of Mach number on measured C_D versus α, Re=12x10^6, T=117K. (Note: this analysis is based on preliminary test data)



a) Baseline configuration *b) Appendix C Leading Edge Ice* c) Appendix O Leading Edge Ice

Figure 17 – The effect of Mach number on measured C_M versus α, Re=12x10^6, T=117K. (Note: this analysis is based on preliminary test data)

A comprehensive and more detailed analysis of the experimental data is required to explain all of the subtle physical effects of leading edge ice on high lift wing performance, and the effect of Reynolds number and Mach number, but this paper provides a first presentation of the data to the aerospace community and an indication of the rich flow physics involving aircraft icing that needs to be better understood. Further papers from the ICED-CRM project will present the runback ice study, and will analyze the leading-edge ice effect in more detail, employing high resolution CFD both to highlight the flow characteristics and also to answer the question, what CFD methods can best predict these effects, if at all?

4. Conclusions

- The interaction effect of leading-edge ice on protected slat surfaces, together with runback ice behind un-protected surfaces, which was originally a goal of this study but was dropped from the test program in order to mitigate risks, still needs to be studied experimentally.

- Cryogenic testing is very difficult, particularly involving the bonding of artificial ice shapes. In this project, metal additively manufactured or 3D printed scaled down ice parts have been found to be superior to corresponding silicon molded parts in their ability to survive multiple cool-downs and warm-ups necessary to undertake productive cryogenic tests. The surface bonding method is critical, with epoxy with the correct thermal expansion properties being essential.
- Leading edge ice significantly degrades aerodynamic performance of a civil aircraft in high lift configuration at low speed. Appendix O ice data was found to degrade C_{Lmax} even further than with Appendix C ice on the unprotected slat leading edges. Such leading-edge ice also extends the range of force and moment hysteresis, significantly reducing the angle of attack on the pitch down, at which recovery to linear force trends occurs.
- The study will provide a new validation dataset for a representative and publicly available large transport aircraft geometry, once the data are finalised. In doing so, it will improve understanding of supercooled large droplet icing effects, support better validation of computational tools, and helps strengthen the experimental foundation for future Appendix O certification method.

5. References

[1] K. Hood and I. Douglas, Manufacturers Icing Certification Group, "AIA Research Needs for Appendix O Supercooled Large Drop Icing with MVD Greater Than 40mm to Support Airframe Ice Accretion Certification – A Gap Analysis," Aerospace Industries Association, 2026.

[2] C. Bosetti and B. P. Paul, “The Current State and Future Goals of Icing Analysis Tools and Their Impact on Aerodynamic Design, SAE International Conference on Aircraft and Engine Icing and Ground Deicing, 2011.

[3] M. B. Bragg, A. P. Broeren, and L. A. Blumenthal, “Iced-Airfoil Aerodynamics,” Progress in Aerospace Sciences, vol. 41, no. 5, pp. 323–362, 2005.

[4] F. T. Lynch and A. Khodadoust, “Effects of Ice Accretions on Aircraft Aerodynamics,” Progress in Aerospace Sciences, vol. 37, no. 8, pp. 669–767, 2001.

[5] Federal Aviation Administration, “14 CFR Part 25, Appendix C—Atmospheric Icing Conditions" Code of Federal Regulations.

[6] European Union Aviation Safety Agency, “Certification Specifications and Acceptable Means of Compliance for Large Aeroplanes, CS-25, Appendix C—Atmospheric Icing Conditions.”

[7] Federal Aviation Administration, “14 CFR Part 25, Appendix O—Supercooled Large Drop Icing Conditions" Code of Federal Regulations.

[8] European Union Aviation Safety Agency, “Certification Specifications and Acceptable Means of Compliance for Large Aeroplanes, CS-25, Appendix O—Supercooled Large Drop Icing Conditions.”

[9] P. Trontin, A. Kontogiannis, G. Blanchard and P. Villedieu. “Description and Assessment of the New ONERA 2D Icing Suite IGLOO2D”. AIAA Paper 2017-3417, 2017.

[10] National Transportation Safety Board, In-Flight Icing Encounter and Loss of Control, Simmons Airlines, d.b.a. American Eagle Flight 4184, ATR-72-212, Roselawn, Indiana, October 31, 1994, Aircraft Accident Report NTSB/AAR-96/01, 1996.

[11] D. S. Lacy and A. J. Sclafani, “Development of the High Lift Common Research Model: A Representative High Lift Configuration for Transonic Transports,” AIAA Paper 2016-0308, 2016.

[12] A. P. Broeren, H. E. Addy, M. B. Bragg, G. T. Busch, D. Guffond, and E. Montreuil, “Swept-Wing Ice Accretion Characterization and Aerodynamics,” AIAA/NASA technical publication, 2013–2014.

[13] A. P. Broeren, M. G. Potapczuk, S. Lee, A. M. Malone, B. P. Paul, and B. S. Woodard, Experimental and Computational Icing Simulation for Large Swept Wings, NASA technical publication, 2022.

[14] S. G. Cober, G. A. Isaac, and J. W. Strapp, “Characterizations of Aircraft Icing Environments that Include Supercooled Large Drops,” Journal of Applied Meteorology, vol. 40, no. 11, pp. 1984–2002, 2001.

[15] A. P. Broeren, E. A. Whalen, G. T. Busch, and M. B. Bragg, “Aerodynamic Simulation of Runback Ice Accretion,” Journal of Aircraft, vol. 47, no. 3, pp. 924–939, 2010.

[16] G. E. C. Fujiwara, M. B. Bragg, and A. P. Broeren, “Comparison of Computational and Experimental Ice

Accretions of Large Swept Wings," Journal of Aircraft, vol. 57, no. 2, pp. 342–359, 2020.

[17] A. P. Broeren, T. A. Ozoroski, C. E. Porter and Kolleen K. Hood. "Aerodynamic Effect of Artificial Ice Shapes on the 5.2% Scale Semispan High-Lift Common Research Model in the NASA National Transonic Fac

[18] M. Ertsgaard and C. S. Winski. "Development of NASA 2.7% Semispan and Full Span High Lift Common Research Models (CRM-HL)", AIAA 2025-3460. AIAA Aviation Forum and Ascend 2025. July 2025.

6. Contact Author Email Address

Mail to: simon.prince@cranfield.ac.uk;

7. Copyright Statement

The authors confirm that they, and/or their company or organization, hold copyright on all of the original material included in this paper. The authors also confirm that they have obtained permission, from the copyright holder of any third party material included in this paper, to publish it as part of their paper. The authors confirm that they give permission, or have obtained permission from the copyright holder of this paper, for the publication and distribution of this paper as part of the ICAS proceedings or as individual off-prints from the proceedings.

8. Acknowledgements

This work was funded by the UK Department for Science, Innovation and Technology (DSIT) and the Engineering & Physical Sciences Research Council (EPSRC), and supported by Boeing, Airbus, NASA and the European Transonic Wind Tunnel (ETW), with input from the UK Aerospace Technology Institute (ATI), the National Wind Tunnel Facility (NWTF) and the US Federal Aviation Administration.

The authors would like to acknowledge the following people from the respective organizations listed below for their contributions and support which made this research possible:

- Airbus: Dietmar Meißner, Matthew Bees, Olivier Blesbois, Elliot Kane, & Angela Styles
- Boeing: Sean Ali, Soroush Yazdani, Ashley Evans, Neville Koh, Alecsandra Court, Farshad Soleimaninia
- NASA: James O'Shaughnessy, Brandon Caudill, Sheida Hosseinei
- ETW: Thomas Baumgart & the wider team at ETW.